

Article

Experimental and Numerical Study of the Nonlinear Evolution of Regular Waves over a Permeable Submerged Breakwater

Ping Wang ^{1,2} , Kezhao Fang ^{2,3,*}, Gang Wang ³, Zhongbo Liu ⁴  and Jiawen Sun ¹

¹ National Marine Environmental Monitoring Center, State Environmental Protection Key Laboratory of Marine Ecosystem Restoration, Dalian 116023, China; wangping@nmemc.org.cn (P.W.); jwsun@nmemc.org.cn (J.S.)

² Key Laboratory of Coastal and Offshore Engineering, Faculty of Infrastructure Engineering, Dalian University of Technology, Dalian 116024, China

³ Marine Ecological Restoration and Smart Ocean Engineering Research Center of Hebei Province, Qinhuangdao 066000, China; wanggang8080@163.com

⁴ College of Transportation Engineering, Dalian Maritime University, Dalian 116024, China; liuzhongbo@dlmu.edu.cn

* Correspondence: kfang@dlut.edu.cn

Abstract: The permeable submerged breakwater has gained popularity in recent days due to its merits of reducing incident wave energy without negatively impacting the aesthetics of the ocean view and allowing for water exchange. However, the effect of porosity on wave nonlinearity and turbulence motion close to the water/structure interface is not well resolved in the literature. This paper presents an experimental and numerical study of regular wave propagation over a permeable submerged breakwater with a wide top width. The laboratory experiments were conducted in a wave flume and included 45 test cases. The numerical simulations were performed utilizing validated olaFoam. The results show that the nonlinearity of the waves on the permeable submerged breakwater is weak, which can effectively suppress and reduce the second harmonic waves. A large amount of turbulent kinetic energy exists at the interface between the permeable submerged breakwater and the water body, which helps to dissipate wave energy. For the wider permeable submerged breakwater in this paper, the wave dissipation capacity is greatest when the porosity is between 0.2 and 0.3, and as the length of the breakwater increases, the energy transmission coefficient decreases, and the energy dissipation coefficient increases. Better wave attenuation is achieved when the permeable submerged breakwater has a certain porosity and a large width.

Keywords: permeable submerged breakwater; wave; nonlinearity; numerical simulation



Citation: Wang, P.; Fang, K.; Wang, G.; Liu, Z.; Sun, J. Experimental and Numerical Study of the Nonlinear Evolution of Regular Waves over a Permeable Submerged Breakwater. *J. Mar. Sci. Eng.* **2023**, *11*, 1610. <https://doi.org/10.3390/jmse11081610>

Academic Editor: Cristiano Fragassa

Received: 10 July 2023

Revised: 3 August 2023

Accepted: 15 August 2023

Published: 17 August 2023



Copyright: © 2023 by the authors. Licensee MDPI, Basel, Switzerland. This article is an open access article distributed under the terms and conditions of the Creative Commons Attribution (CC BY) license (<https://creativecommons.org/licenses/by/4.0/>).

1. Introduction

Submerged breakwaters are frequently utilized in coastal protection due to their submergence beneath the water and little influence on the water flow and coastal environment [1]. Since 1980, submerged breakwaters have been utilized in Italy to protect the coastline [2], and by 1996, more than 50 such protection systems had been established. Additionally, many old emerged breakwaters have been or are being converted into submerged breakwaters in Italy [3–5]. Permeable submerged breakwaters are less expensive than impermeable submerged breakwaters, and the pores in the permeable materials produce a damping effect and promote the dissipation of wave energy, which is effective in protecting the shore and coastal structures [6,7]. It is thus essential for the scientific community to gain a comprehensive understanding of wave propagation over permeable submerged breakwaters [8].

Laboratory experiments are the main method for studying the interaction between waves and submerged breakwaters; e.g., Chang et al. [9] conducted a series of experiments to study wave reflection, transmission, and dissipation properties over rectangular submerged breakwaters. Li et al. [10] conducted both analytical and laboratory experiments

on the interaction between regular waves and a submerged breakwater. Dattatri et al. [11] experimentally investigated the effect of permeability on wave height dissipation and confirmed the advantages of permeable submerged breakwaters. Losada et al. [12] experimentally found that permeable structures can increase the effective water depth and reduce the chance to generate high harmonics. Ting et al. [13] pointed out that the bottom width of a permeable breakwater has a limited effect on wave reflection and transmission. Peng et al. [14] studied the effect of permeable submerged breakwaters on wave nonlinearity utilizing the measurement data set from the DELOS project. They developed a set of empirical formulas to calculate the wave skewness and asymmetry at the incident and lee sides of submerged breakwaters. Zou and Peng [15] further improved these equations and summarized the general law of the variation of the skewness and asymmetry along a permeable breakwater. Wu and Hsiao [6] studied the variation of isolated waves on a permeable submerged breakwater composed of smooth spheres. They found that turbulence intensity at the incident side of the permeable breakwater is greater than that at the transmission side, the wave reflection coefficient decreases as the porosity increases and the transmission coefficient decreases, and the wave height dissipation increases with an increase of breakwater width.

Numerical simulation is also an important tool for the study of the hydrodynamic properties of permeable submerged breakwaters. Boussinesq-type equations developed originally for describing open water waves over a solid seabed have been extended to consider wave propagation in or over porous structure, e.g., [16–23]. However, these models are essentially depth-integrated and fail to accurately describe the distribution of flow velocity along the water depth, let alone the flow details after wave breaking. On the other hand, Liu et al. [24] proposed a numerical model based on the Reynolds-averaged Navier–Stokes (RANS) equations and the volume of fluid (VOF) method. This model is spatially averaged for porous flow with the assumption that the turbulence inside the porous media is negligible. Hsu et al. [25] took the volume average of the RANS equations along with the k – ϵ model over a control volume to solve the turbulence effects in a clear fluid and porous flow. This set of formulas is widely used to model macroscopic porous media flow in coastal-related problems, e.g., [26–28]. A set of volume-averaged Reynolds-averaged Navier–Stokes (VARANS) equations coupled with k – ϵ and shear stress transport (SST) turbulence models was derived by Jesus et al. [29] and then extended to 3D coastal-related applications by Higuera et al. [30] who introduced these equations into OpenFOAM to simulate flow in a permeable medium, and it was verified in a 3D experiment by Lara et al. [31]. Wu et al. [32] presented a 3D large-eddy simulation model with macroscopic model equations of a porous flow to investigate solitary waves interacting with permeable breakwaters and found that the results obtained with macroscopic and microscopic modeling both fit the measurements well in terms of the free surface elevations and velocity fields. In a word, the RANS-based models have become state-of-the-art tools in simulating coastal hydrodynamics related to various types of porous structures.

The majority of the experimental and numerical results mentioned above focus on the hydrodynamics over the breakwaters with normal top widths. In practical applications, the width of submerged breakwaters is usually many times the size of an emergent one in order to achieve a better shielding effect. The placement of such a large structure changes the local water depth and significantly affects the transformation of the incident waves, especially modifying the distribution of wave nonlinearities [33]. Regarding this issue, there has been an increasing interest in studying the nonlinear evolution of waves over broad underwater sills in recent years using analytical solutions [34], physical experiments (e.g., [35,36]), and numerical simulations (e.g., [37,38]). However, the broad sills in these studies are impermeable. Pore resistance from a permeable medium is another key factor that controls the wave dissipation capability of a submerged breakwater. The effect of the porosity of a wide submerged breakwater on wave nonlinearity and turbulence motion close to the water/structure interface is not well-resolved yet.

In this paper, we investigated the effect of the permeability of a wide submerged breakwater on nonlinear wave evolution and wave dissipation capacity. The rest of the paper is laid out as follows. The new physical experiment is detailed in Section 2. Section 3 briefly describes the olaFoam model. The analysis of the experimental data and numerical results are given in Section 4 and Section 5, respectively. Conclusions are drawn in Section 6.

2. Physical Experiments

The experiment was conducted in a wave flume at the State Key Laboratory of Coastal and Offshore Engineering, Dalian University of Technology. The flume tank is 56 m long, 3 m wide, and 1 m deep. The flume has a paddle-style wave maker that can generate regular waves with a maximum height of 0.3 m and periods between 0.5 and 5.0 s. The experimental setup is shown in Figure 1. A permeable submerged breakwater consisting of 5 layers of 5 cm glass spheres stacked in a body-centered cubic style (i.e., 4 spheres in the lower layer and 1 sphere in the upper layer) is positioned 25.62 m away from the wave paddle. The submerged breakwater has a height of 19 cm, a top width of 4 m, and slopes of 1:2 and 1:07 on the incident and lee sides, respectively. The porosity of the submerged breakwater is 0.32. Impermeable submerged breakwater of the same size is also used in the experiments for comparison aims. A 5 m wide plastic wave absorber is placed at the end of the flume to avoid wave reflection.

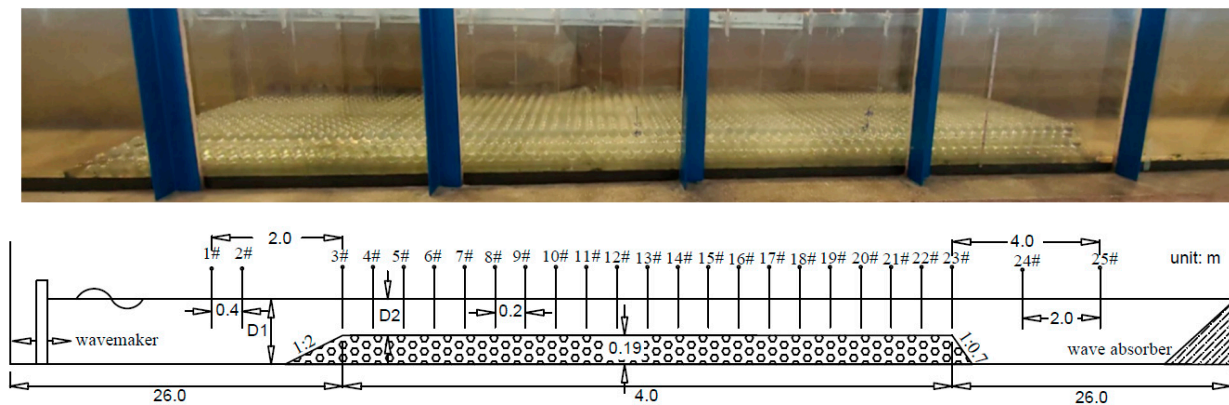


Figure 1. Setup of physical experiments; 1#~25# represent the locations of the wave gauges.

Twenty-five wave gauges were used to measure the free surface elevation along the flume, and their locations are sketched in Figure 1. Wave gauges 1–2# and 24–25# were positioned in front and behind the breakwater, respectively, to measure the wave height of incident and transmitted waves. The rest wave gauges cover the top of breakwater with an interval of 0.2 m to measure the wave height variation over the breakwater. All gauges were calibrated before experiments to ensure linearity and stability. The sampling rate of the free surface elevation was set to 50 Hz.

The submerged breakwater mainly takes effect by causing breaking as waves enter the shallower water depth. However, in case of high water levels (due to sea level rise or storm surge), there is a possible scenario that waves do not break. In this case, the submerged breakwater enhances the nonlinear transformation of the incident waves, and this is exactly the issue we focus on. Table 1 lists 45 test cases used in the experiments with a combination of different water depths and non-breaking incident waves. In Table 1, D_1 is water depth at the wave maker, D_2 is water depth on the submerged breakwater, T is wave period, L is wavelength, and H is wave height. Each case listed in Table 1 was run three times to ensure repeatability, and the wave maker lasted two minutes for each case.

Table 1. Test cases of physical experiments.

Case	D_1 (cm)	D_2 (cm)	T (s)	L (m)	H (cm)
1~6	30	11	0.8	0.96	2, 3, 4, 5, 6, 7
7~11	30	11	1.2	1.77	2, 3, 4, 5, 6
12~15	30	11	1.5	2.34	2, 3, 4, 5
16~19	40	21	0.9	1.22	3, 5, 7, 9
20~23	40	21	1.2	1.94	3, 5, 7, 9
24~27	40	21	1.8	3.27	3, 5, 7, 9
28~30	40	21	2.5	4.74	3, 5, 7
31~38	50	31	1	1.51	4, 7, 10, 13
35~38	50	31	1.5	2.83	4, 7, 10, 13
39~42	50	31	1.8	3.57	4, 7, 10, 13
43~45	50	31	2.5	5.24	4, 7, 10

3. Numerical Model

3.1. Governing Equations

The OpenFOAM model was chosen for the numerical simulations, which deals with the flow problems in pore media in two ways, i.e., microscopi– and macroscopic methods. The microscopic approach requires that the internal structure of the porous material is all presented during discretization, but this is unrealistic. The macroscopic approach is based on the average behavior of the flow within the pore material, and the volume-averaging Navier–Stokes equation allows the pore region to be considered a continuous medium. In this paper, we follow the second approach and used olaFoam to perform the numerical simulations, which solves the three-dimensional VARANS equation by the finite volume discretization method and the VOF method.

The mass conservation equation, the momentum conservation equation, and the VOF functional convection equation read as [29]:

$$\frac{\partial}{\partial x_i} \frac{u_i}{u} = 0 \tag{1}$$

$$\frac{\partial}{\partial t} u_i + u_j \frac{\partial}{\partial x_j} \frac{u_i}{n} = -\frac{n}{\rho} \frac{\partial}{\partial x_i} p + n g_i + n \frac{\partial}{\partial x_j} \left(v \frac{\partial}{\partial x_i} \frac{u_i}{n} \right) - a u_i - b u_i |u_i| - c \frac{\partial}{\partial t} u_i \tag{2}$$

$$\frac{\partial \alpha_1}{\partial t} + \frac{\partial}{\partial x_i} \frac{u_i}{n} \alpha_1 = 0 \tag{3}$$

$$\rho = \alpha_1 \rho_1 + (1 - \alpha_1) \rho_2 \tag{4}$$

$$v = \alpha_1 v_1 + (1 - \alpha_1) v_2 \tag{5}$$

where $(u_i, i = 1,2,3)$ is the extended mean velocity or Darcy velocity, n is the porosity, ρ is the density, ρ_1 is the density of water, ρ_2 is the density of air, p is the pressure, g is the acceleration of gravity, v is the kinematic viscosity, v_1 and v_2 are the kinematic viscosities of water and air, respectively, and α_1 is the phase function of the VOF method defined as the amount of water in a single grid. If $\alpha_1 = 1$, the grid is filled with water, if $\alpha_1 = 0$, the grid is filled with air, and if α_1 is between 0 and 1, the grid belongs to the free water surface. The last three terms of Equation (2) are used to account for physical problems that cannot be solved by volume averaging methods, namely friction, pressure, and additional mass due to the presence of porous media, with coefficients a , b , and c depending on the physical material properties of the porous media.

Higuera [30] improved the VARANS equation and introduced it into the IHFoam, changed the Darcy velocity of the continuum equation to the intrinsic velocity, and made

an adjustment to Equation (2) by multiplying both sides of the equation by ρ and dividing by the porosity n in the following form:

$$U^* = \frac{U}{n} \tag{6}$$

$$(1 + c) \frac{\partial}{\partial t} \frac{\rho u_i}{n} + \frac{u_j}{n} \frac{\partial}{\partial x_j} \frac{\rho u_i}{n} = - \frac{\partial}{\partial x_i} p + \rho g_i + \frac{\partial}{\partial x_j} \left(\mu \frac{\partial}{\partial x_i} \frac{u_i}{n} \right) - A \frac{u_i}{n} - B \frac{u_i}{n} \left| \frac{u_i}{n} \right| \tag{7}$$

where $A = \rho a$, and $B = \rho n b$. When the Reynolds number of the fluid is small, the flow resistance is mainly related to A and vice versa to B . The equations for A and B were proposed by Engelund [39] and modified by Van Gent [40] as follows:

$$A = \alpha \frac{(1 - n)^3}{n^2} \frac{\mu}{D_{50}^2} \tag{8}$$

$$B = \beta \left(1 + \frac{7.5}{KC} \right) \frac{1 - n}{n^2} \frac{\rho}{D_{50}} \tag{9}$$

where D_{50} is the median particle size of the porous medium, KC is the Keulegan–Carpenter number indicating the additional friction due to oscillations and instabilities defined as $(T_0 u_M) / (D_{50} n)$, T_0 is the oscillation period, and u_M is the maximum oscillation velocity. α , β , and c are dimensionless coefficients, and they are set to be 500, 2, and 0.34 according to previous studies (Jesus [29], Jensen et al. [41]).

3.2. Turbulence Model

Reynolds time-averaged models are the most widely used numerical models of turbulence, such as $k-\epsilon$ and $k-\omega$ models. $k-\epsilon$ is a high Reynolds number model that can obtain better results in simulating turbulence away from sidewalls, and the $k-\omega$ model is a low Reynolds number model that is more suitable for the boundary layer problem under various pressure gradients, but it is more difficult to converge than the $k-\epsilon$ model. In this paper, the turbulence calculation adopts the $k-\omega$ SST model developed by Menter et al. [42], which is similar to the $k-\omega$ model in that it retains the characteristics of the low Reynolds number model in the vicinity of the boundary wall, but its convergence can be comparable to that of the $k-\epsilon$ model, and its expression is as follows:

$$\frac{\partial k}{\partial t} + \frac{\partial u_j k}{\partial x_j} - \frac{\partial}{\partial x_j} \left[(v + \sigma_k v_t) \frac{\partial k}{\partial x_j} \right] = P_k - \beta^* \omega k \tag{10}$$

$$\frac{\partial \omega}{\partial t} + \frac{\partial u_j \omega}{\partial x_j} - \frac{\partial}{\partial x_j} \left[(v + \sigma_\omega v_t) \frac{\partial \omega}{\partial x_j} \right] = \frac{\gamma}{v_t} G - \beta \omega^2 + 2(1 - F_1) \frac{\sigma_\omega}{\omega} \frac{\partial k}{\partial x_j} \frac{\partial \omega}{\partial x_j} \tag{11}$$

$$P_k = \min(G, 10\beta^* k \omega) \tag{12}$$

$$G = v_t \frac{\partial u_i}{\partial x_j} \left(\frac{\partial u_i}{\partial x_j} + \frac{\partial u_j}{\partial x_i} \right) \tag{13}$$

$$v_t = \frac{a_1 k}{\max(a_1 \omega, S F_2)} \tag{14}$$

where k denotes the turbulent kinetic energy, P_k denotes the generating term of k , v denotes the kinematic viscosity, v_t denotes the kinematic viscosity of the turbulent flow, ω denotes the specific dissipation rate, S denotes the mean strain rate of the flow, $\beta^* = 0.09$, and $a_1 = 0.31$. F_1 and F_2 are mixing functions with F_1 going to 1 close to the sidewalls (activating the $k-\epsilon$ model) and 0 away from the sidewalls (activating the modes $k-\omega$), and the σ_k , σ_ω , β , and γ are determined by a mixing equation.

Larsen and Fuhrman [43], Mayer and Madsen [44], and Devolder et al. [45] pointed out that numerical instability can cause excessive growth of turbulent kinetic energy, which causes artificial wave numerical dissipation and unrealistic attenuation of the wave height; for this reason, a correction term was added by Devolder et al. [45] in the $k-\omega$ SST model (Equation (10)), and the corrected turbulence level of the flow field matches well with the experimental measurements and significantly improves the wave attenuation along the flume, with the expression as follows:

$$G_b = \frac{v_t}{\sigma_t} \frac{\partial \rho}{\partial x_j} g_j \tag{15}$$

3.3. Boundary Conditions

The numerical model adopted the boundary wave-generated method. Based on the linear wave theory, the displacement and velocity of the wave-making paddle are calculated through the transfer function relationship between the wave height and the stroke of the wave-making paddle. The formulas are as follows:

$$H_s = \frac{H}{S} = \frac{4\sinh^2(kd)}{2kd + \sinh 2kd} \tag{16}$$

$$X(t) = \frac{S}{2} \sin(\omega t) \tag{17}$$

$$U(t) = \frac{S}{2} \omega \cos(\omega t) \tag{18}$$

where H_s is the transfer function, H is the wave height of the regular wave, S is the wave paddle displacement, k is the wave number, d is the water depth, t is the time, and ω is the circular frequency of the target wave.

At the end of the flume, the damping layer wave dissipation method is used where a source term is added to the momentum equation to gradually attenuate the velocity of the waves in the damping zone. And the active wave absorption method is used in the vicinity of the wave-making paddle. The wavemaker paddle displacement is corrected by calculating the correction required to eliminate secondary reflected waves, and the modified formulas are given by:

$$X(t) = \frac{S}{2} \sin(\omega t) + \int u_{corr} dt \tag{19}$$

$$u_{corr} = -\frac{\omega}{H_s} (\eta_m - \eta_0) \tag{20}$$

where u_{corr} is the corrected speed of the wavemaker paddle, and η_m and η_0 are the measured and theoretical wavefronts on the moving boundary, respectively.

A solid wall boundary is used on both sides of the numerical flume, the velocity field satisfies the no-slip condition, and the pressure field satisfies a velocity gradient of 0. The free surface tracking is performed by the VOF method where the position of the grid containing the free surface is obtained after solving for the volume fraction of the phase in the full domain, which leads to the capture of the wave height.

3.4. Coupling Scheme

Since the continuity and momentum equations are coupled together, the velocity and pressure need to be solved coupled. Currently, the coupled solution methods can be divided into the SIMPLE algorithm for steady-state problems and the PISO algorithm for transient problems. Both adopt the idea of "forecast-correction", i.e., obtain the velocity according to the given or assumed pressure, substitute the velocity into the pressure correction equation to obtain the pressure correction value, and use the pressure correction value to improve

the velocity. The olaFoam model algorithm is the PIMPLE algorithm whose idea is to regard each time step as a steady-state problem and solve the problem with the SIMPLE steady-state algorithm, and the advancement of the time step is completed by the PISO algorithm.

4. Analysis of Experimental Results

4.1. Spatial Variation of Wave Height

Figure 2 shows the variation of the wave surface elevation on the permeable and impermeable submerged breakwater topography for Case 10 ($T = 1.2$ s, $H = 5$ cm, $D_1 = 30$ cm). When the wave propagates to the submerged breakwater, the wave undergoes a nonlinear deformation due to the rapid decrease in water depth and the transfer of wave energy to high frequencies. The wave shape changes gradually during this stage with the crest becoming steep and the trough becoming flat. Under the same incident wave conditions (see wave gauge 1#), it can be clearly observed that the wave deformation on the permeable submerged breakwater is significantly smaller than that on the impermeable breakwater. The waves propagating on the impermeable breakwater are more likely to have sub-peaks (e.g., wave gauges 11#, 19#, 23#) and exhibit stronger nonlinearity. It is also clearly observed that permeable breakwaters dissipate more wave energy. Specifically, the wave height at wave gauge 25# is attenuated by nearly 54% when penetrating the submerged breakwater, while the wave height after the impermeable submerged breakwater is only attenuated by 14%.

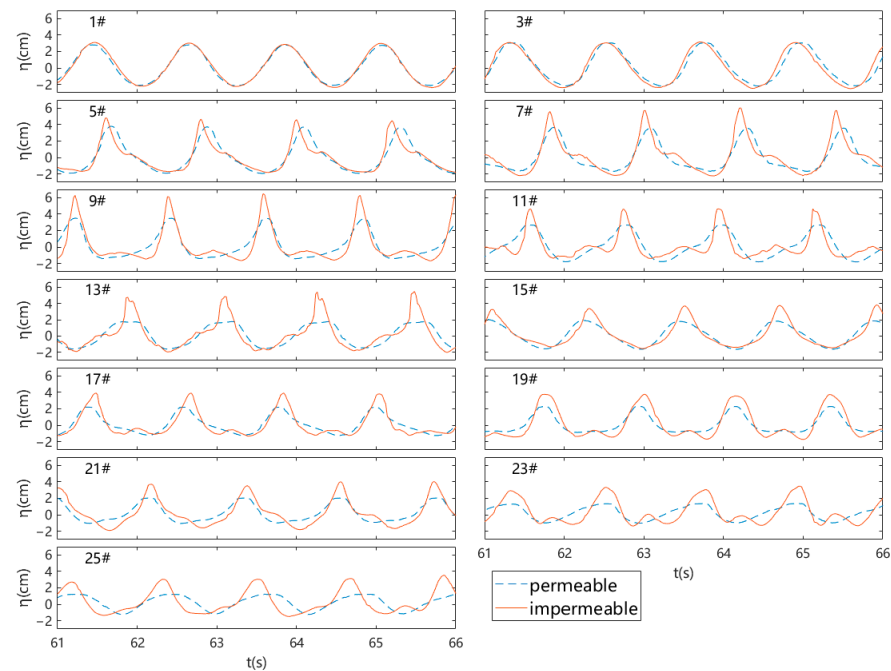


Figure 2. Time series of free surface elevation at different wave gauges (Case 10, $T = 1.2$ s, $H = 5$ cm, $D_1 = 30$ cm).

Figures 3 and 4 show the variation of the wave height for test cases with $D_1 = 30$ (Case 1–15) cm and $D_1 = 50$ cm (Case 31–45), respectively. In the figures, the horizontal coordinates start from the position of wave height gauge 1#, and the vertical coordinates are the ratio of the wave height to the wave height from the first gauge.

As shown in Figure 3, the wave height variation on the permeable submerged breakwater shows a smoother decreasing trend, while the wave height variation on the impermeable submerged breakwater has a large fluctuation, and the decreasing trend is not obvious. The wave height attenuation on the permeable submerged breakwater is significantly higher, and the damping effect caused by the pore space cannot be ignored. The attenuation of wave height on impermeable submerged breakwaters is extremely limited, and even no

attenuation occurs when the wave height is small. And as the wave height increases, the waves on the impermeable submerged breakwater inevitably happen to break, and the wave height attenuates to a level comparable to that of the permeable submerged breakwater in Cases 6 and 11. As shown in Figure 4, there is a significant drop in wave height attenuation once the water depth is increased to 50 cm compared to those plotted in Figure 3. For some cases with shorter wavelengths and lower wave heights (Case 31), there is no significant difference in the wave dissipation ability of the permeable and impermeable breakwaters.

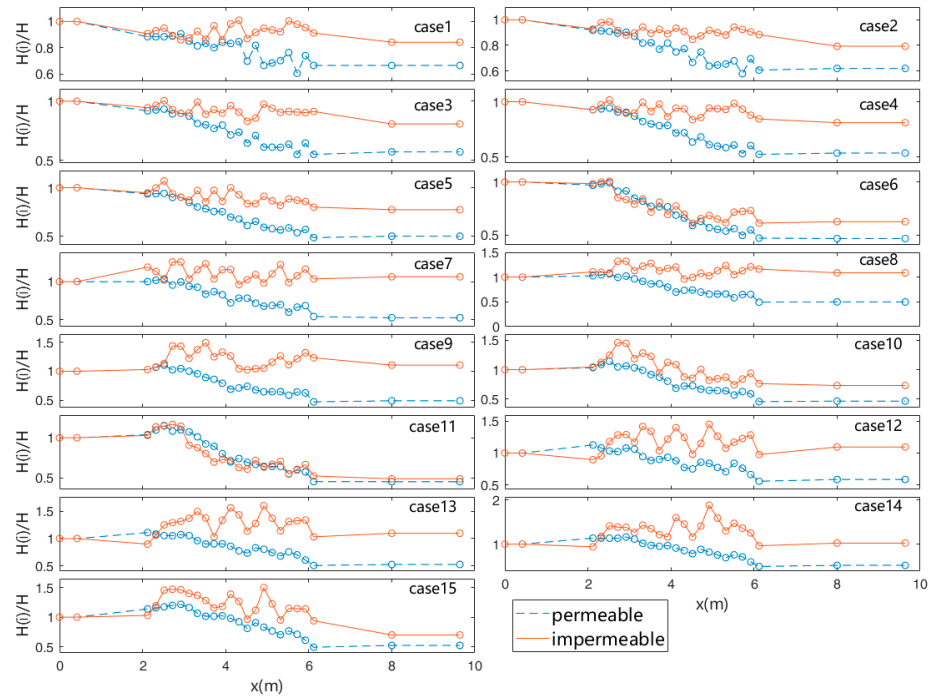


Figure 3. Spatial variation of wave height along wave flume ($D_1 = 30$ cm).

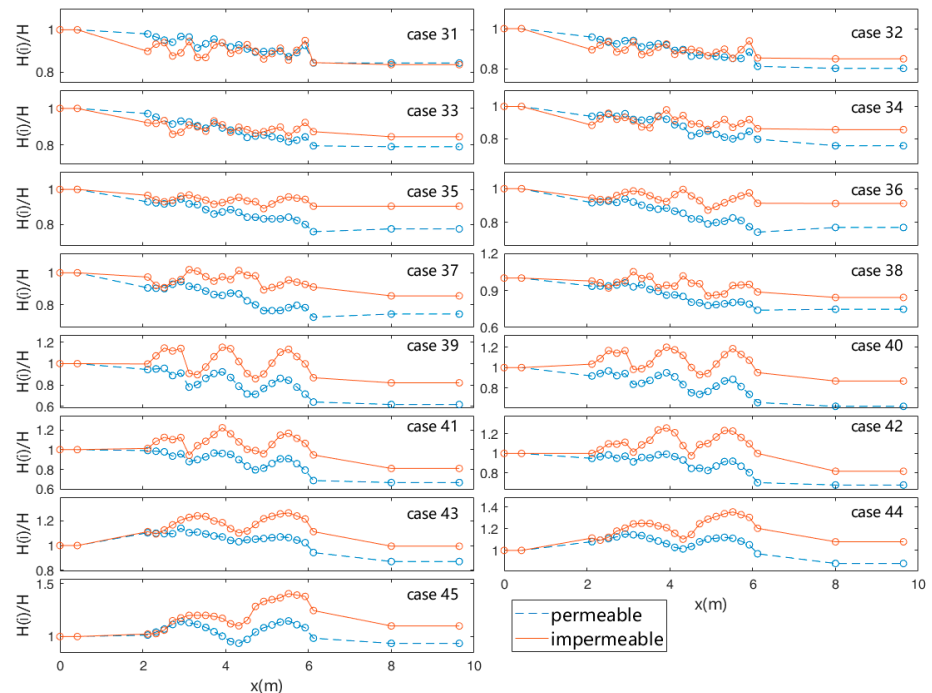


Figure 4. Spatial variation of wave height along wave flume ($D_1 = 50$ cm).

4.2. Transmission Coefficient

The wave attenuation effect of a submerged breakwater is usually quantified by the wave transmission coefficient K_t , which is expressed as the ratio of the transmitted wave height behind the submerged breakwater to the incident wave height at the wave-facing side:

$$K_t = \sqrt{\frac{E_t}{E_i}} = \frac{H_t}{H_i} \tag{21}$$

where E_t and E_i are the transmitted and incident wave energies, and H_t and H_i are the transmitted and incident wave heights, respectively.

Since the difference in wave heights before and after the impermeable submerged breakwater is not significant for non-breaking wave conditions, only the transmission coefficient for test cases with the permeable submerged breakwater was analyzed. The previous study [46] argued that the water depth at the top of the breakwater (D_2) is the most key factor that affects the transmission coefficient. Following this suggestion, the variation of the wave transmission coefficient from the present measurements is plotted with the relative wave height (H/D_2) in Figure 5.

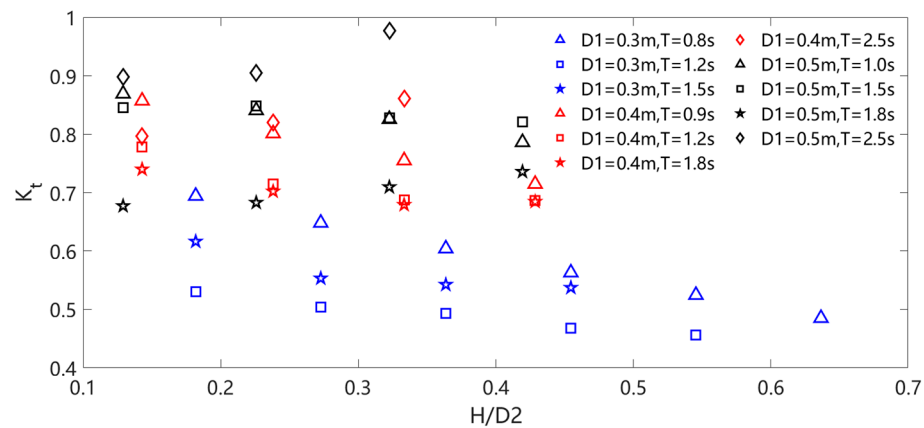


Figure 5. The variation of transmission coefficient with relative wave height.

Figure 5 shows the trend of the wave transmission coefficient with the relative wave height on the permeable submerged breakwater where the relative wave height is the ratio of the incident wave height H to the water depth D_2 at the top of the breakwater. The effect of the water depth at the top of the breakwater on the transmission coefficient is very significant, and for similar relative wave height conditions, the wave conditions with a shallower water depth can achieve lower transmission coefficients; e.g., when the relative wave height $H/D_2 = 0.44$, the transmission coefficient is as low as 0.47 at a water depth of 30 cm, 0.69 at a water depth of 40 cm, and 0.74 at a water depth of 50 cm. In most cases, the wave transmission coefficient decreases as the relative wave height increases, but in some cases, the trend is the opposite, such as the case with a period of 2.5 s at a depth of 40 cm and the cases with periods of 1.8 s and 2.5 s at a depth of 50 cm; the wavelengths of the above cases are 4.74 m, 3.57 m, and 5.24 m, which means that when the wavelength is close to or more than the width of the top of the submerged breakwater, the wave transmission coefficient increases with the increase in relative wave height, probably due to the fact that long waves are more penetrating, and the wave dissipation effect of the submerged breakwater is weakened.

4.3. Spatial Variation of Higher Order Harmonics

After the wave propagates to the submerged breakwater, the wave energy is transferred to high frequencies as the water depth becomes shallower and the nonlinearity is enhanced. After spectral analysis and filtering, the variation of the wave spectrum and amplitude along the water flume can be obtained for each order.

Figure 6 shows the frequency spectrum and the amplitude distribution of each order along the range for Case 8 ($T = 1.2$ s, $H = 3$ cm, $D_1 = 30$ cm). The horizontal coordinate of the wave spectrum is the ratio of the frequency to the main frequency, and the vertical coordinate is the spectral density. The value of the wave spectrum has been processed, and the original spike has been changed to a flat top in order to show its spectral value more clearly. The horizontal coordinate of the amplitude distribution of each order is the position of wave height gauge 1#, and the vertical coordinate is the amplitude corresponding to each order frequency. From the results of wave height gauge 1# in the figure, the reflection phenomenon occurring in front of the permeable submerged breakwater is weaker compared to the impermeable submerged breakwater under Case 8. At wave height gauge 7# ($x = 2.92$ m), the waves both showed a significantly high-frequency component on two breakwaters, but the high frequencies on the permeable breakwaters were less, and the third and fourth frequency components were not obvious.

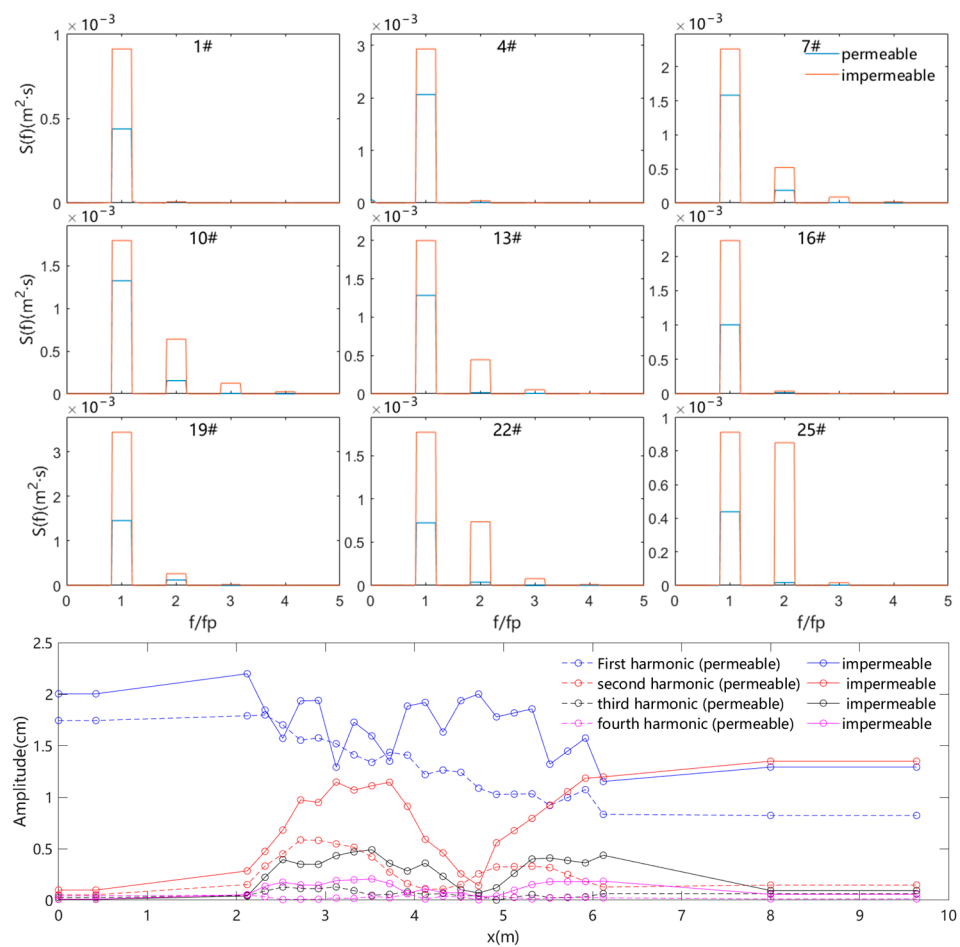


Figure 6. Energy spectrum at different wave gauges and spatial variation of harmonic amplitude along the flume (Case 8).

From wave height gauge 13# ($x = 4.12$ m), the high-frequency component on the permeable breakwater is very weak, and the main frequency is dominant after this point. At the middle and back of the submerged breakwater (at gauge 16#), the high-frequency waves on the impermeable submerged breakwater first decrease and then increase, and the proportion of the second frequency gradually increases; at the back of the impermeable submerged breakwater, the amplitudes of the second frequency and the main frequency are basically the same, while the third and fourth frequency components basically disappear. From the above phenomenon, it is easy to see that the existence of pore space can effectively suppress the transfer of wave energy to high frequencies.

Figure 7 shows the frequency spectrum and the amplitude distribution of each order along the range for Case 11 ($T = 1.2$ s, $H = 6$ cm, $D_1 = 30$ cm). Under this condition, the waves break on the impermeable submerged breakwater, and the wave attenuation is almost the same as that on the permeable breakwater. As can be seen from the above figure, with the increase in incident wave height, the reflection phenomenon obviously occurs at wave height gauge 1#. Like Case 8, the waves on both breakwaters show a significant high-frequency component at wave height gauge 7# ($x = 2.92$ m), and there is almost no significant difference in the four frequencies of the two cases. Between wave height gauge 10# ($x = 3.52$ m) and gauge 22# ($x = 5.92$ m), the wave attenuation effect caused by wave breaking is obvious, and the attenuation amplitude of the main frequency corresponding to the amplitude exceeds the amplitude attenuation due to the pore damping effect. At the same time, the amplitude corresponding to the double frequency of the wave is also significantly attenuated compared to the unbroken cases. Collectively, it seems that under the same conditions, the wave height attenuation amplitude after breaking on the impermeable submerged breakwater is basically the same as that on the unbroken permeable breakwater, and the damping effect of the pore space plays a significant role.

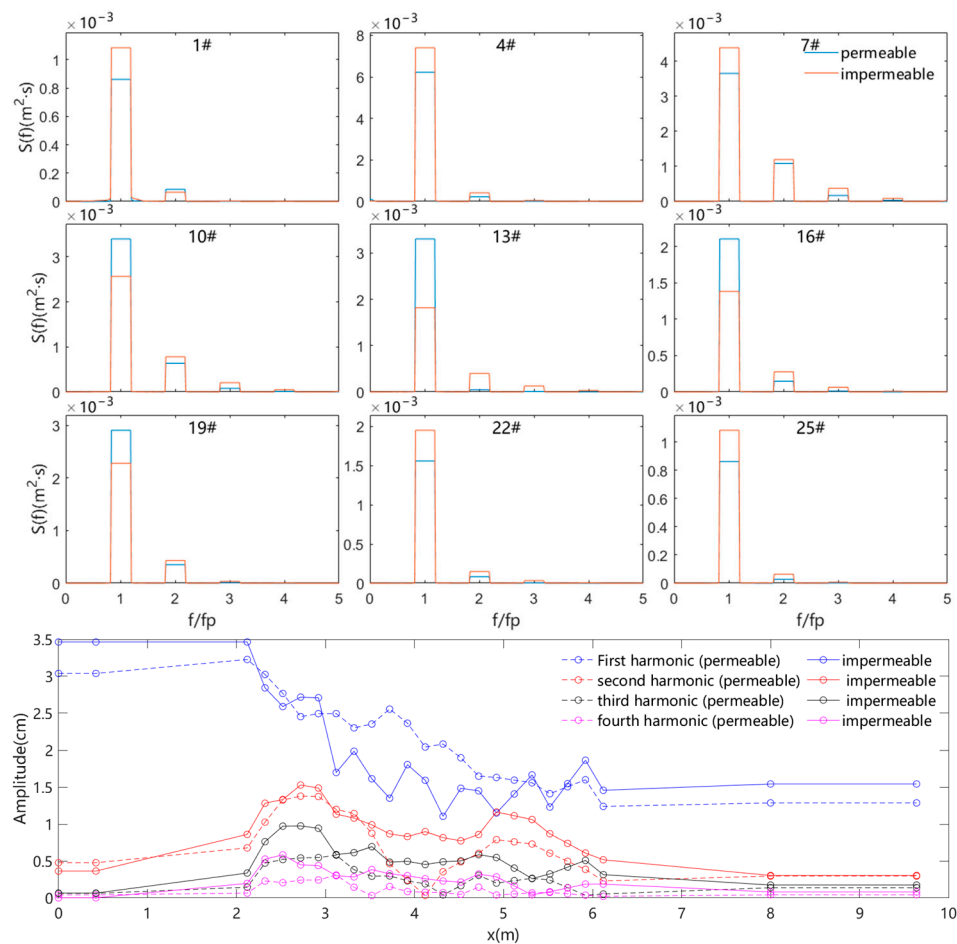


Figure 7. Energy spectrum at different wave gauges and spatial variation of harmonic amplitude along flume (Case 11).

5. Numerical Analysis

The olaFoam solver was used to carry out vertical two-dimensional (2D) simulations to obtain details of the flow field and the turbulent kinetic energy. The numerical wave flume was primarily the same as the physical flume, but for the sake of computation efficiency, the length was reduced to 24 m, and the flume height was set to 0.45 m. The size of the submerged breakwater was identical to that used in the physical experiments and was

positioned 9.62 m away from the wave paddle. The computational domain was discretized using a rectangular grid with resolutions of 1 cm in the horizontal direction and 0.35 cm in the vertical direction, yielding a total of 309,600 grids. The time step of the numerical simulations was 0.02 s.

5.1. The Determination of Resistance Factor

In the VARANS equation, the coefficient c related to inertial acceleration is generally taken as 0.34 by default; the coefficients α and β related to the laminar and turbulent drag forces are referred to the results of Lara et al. [27], which are empirically formulated as follows:

$$\alpha = 4409.22 \times D_{50}^{0.43} \tag{22}$$

$$\beta = 12.27 \times \frac{n^3}{(1 - n)^{1.5}} D_{50}^{-0.1075} \tag{23}$$

According to the above equation, α and β are 1216 and 1.036, respectively. On the other hand, Jensen et al. [41] determined a pair of more generalized α and β values of 500 and 2 based on simulations of pore flow in a variety of flow regimes. To determine the coefficients suitable for this model experiment, 2 groups of 500 and 0.5 and 2000 and 0.5 were added for numerical simulation. The coefficients of α and β were determined by comparing the numerical model and physical experiment; the consistency of the numerical results under different coefficients is better, and most of the cases of the permeable submarine breakwater can be simulated better under the coefficients of 500 and 0.5, and the wave reduction of the permeable breakwater in Cases 14 and 25 is obvious with a small transmission coefficient, and the results of Cases 14 and 25 will be analyzed mainly in the following paper.

Figure 8 shows the simulation results of the wave surface of Case 14 using different parameter combinations. The wave height attenuation of the numerical results obtained by setting β to 0.5 based on the coefficients recommended by Jensen et al. [41] is in general agreement with the measured values. Figure 9 shows the numerical results for Case 25 based on the values of the parameters α and β of 500 and 0.5, and the amplitude and phase of the numerical simulation are in good agreement with the measurement, which further shows the reasonableness of the set of parameter values.

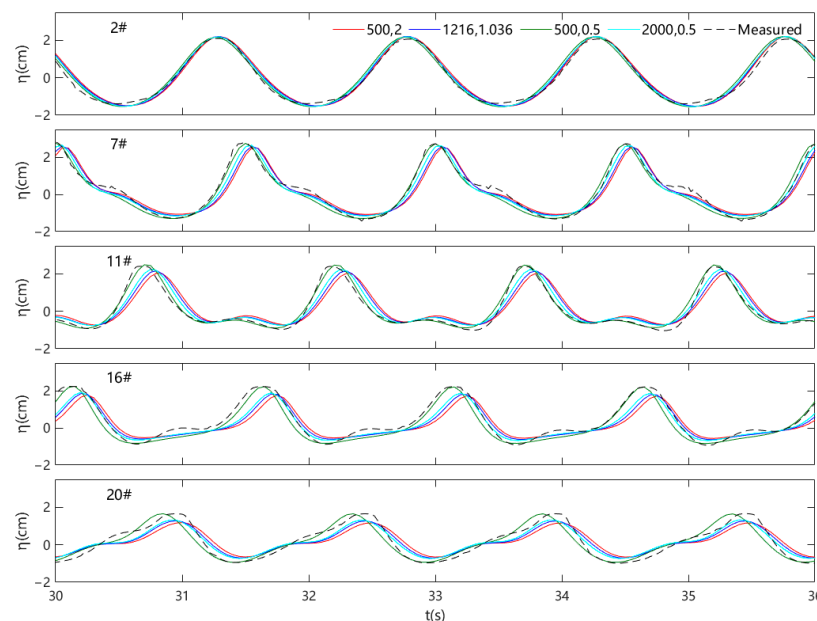


Figure 8. Time series of free surface elevations using different coefficients α and β at different wave gauges (Case 14).

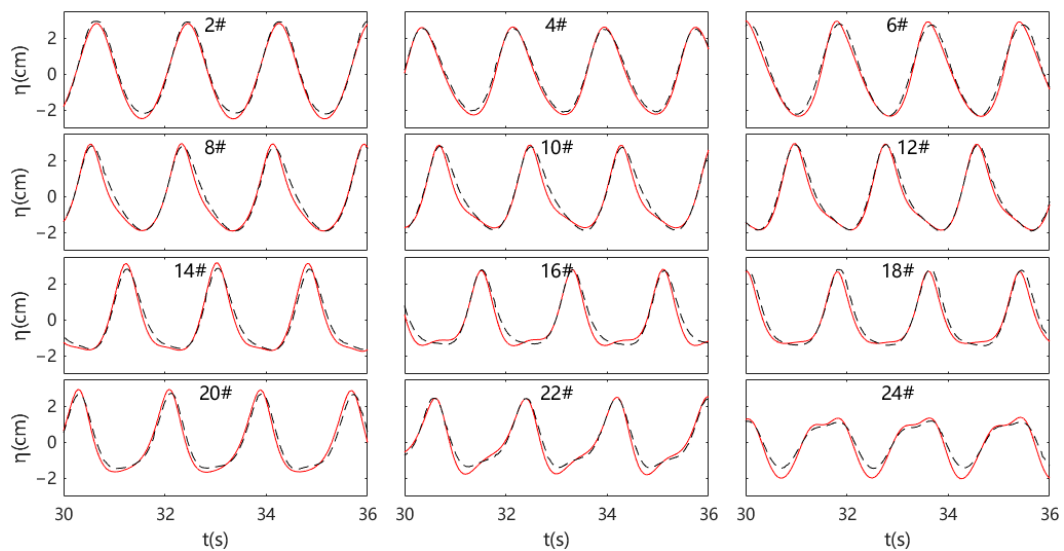


Figure 9. Time series of free surface elevation for regular wave propagation over permeable submerged breakwater at different wave gauges (Case 25, solid lines: simulated, dashed lines: measured).

The simulation results of Case 25 on the impermeable submerged breakwater are shown in Figure 10. The fits of the wave surface at the incident end and the top of the breakwater are both more satisfactory, while the wave height of the numerical results behind the submerged breakwater is higher than the measured value, but overall, the numerical simulation on the impermeable submerged breakwater is still more accurate. In summary, the olaFoam solver can simulate wave attenuation processes on permeable and impermeable submerged breakwaters very well.

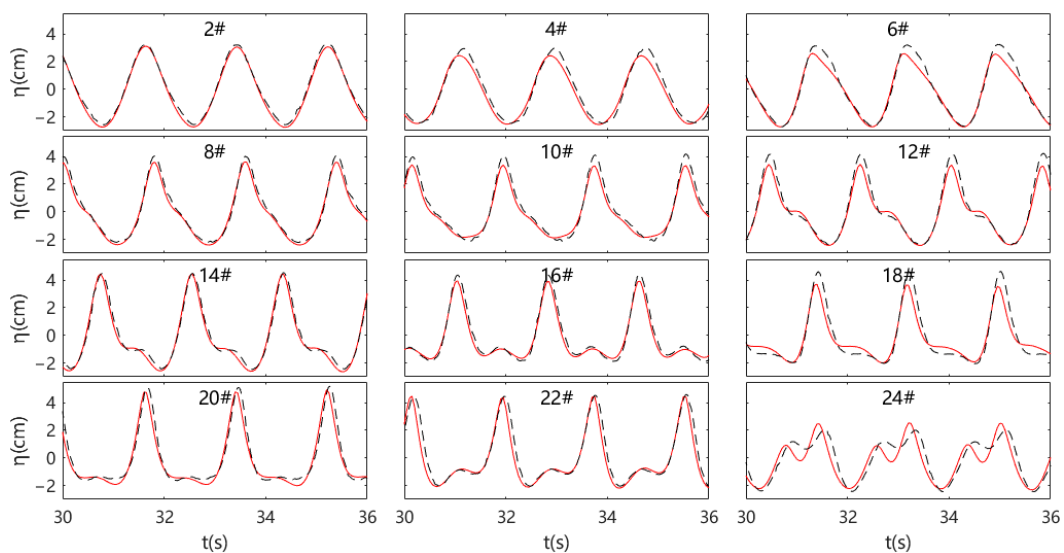


Figure 10. Time series of free surface elevation for regular wave propagation over impermeable submerged breakwater at different wave gauges (Case 25, solid lines: simulated, dashed lines: measured).

5.2. The Flow Field and Turbulent Kinetic Energy

Due to the complex pore distribution inside the permeable breakwater, turbulence is easily formed, which makes it difficult to simulate numerically using microscopic methods, and it is generally studied using macroscopic methods. The numerical results of the permeable and impermeable breakwaters for Case 25 were selected for discussion. Figures 11 and 12 show the flow field of one cycle near the permeable and impermeable

submerged breakwaters, respectively. Because the flow velocity inside the permeable submerged breakwater is small, the arrows in the figures only represent the direction and do not indicate the magnitude of the flow velocity to facilitate a clear observation of the water flow direction.

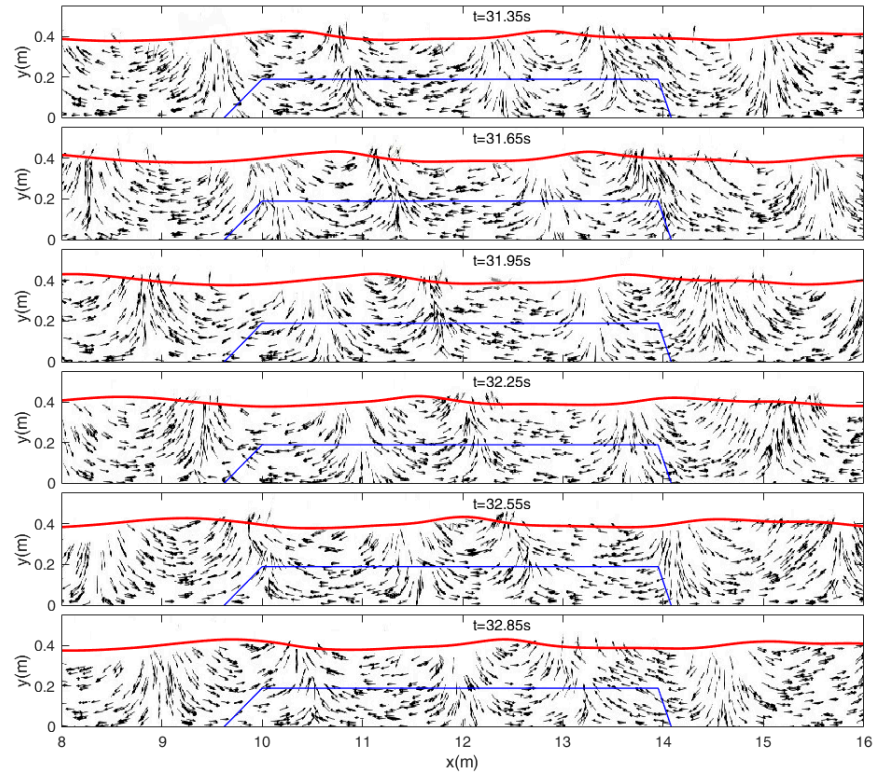


Figure 11. The flow field around permeable submerged breakwater (Case 25).

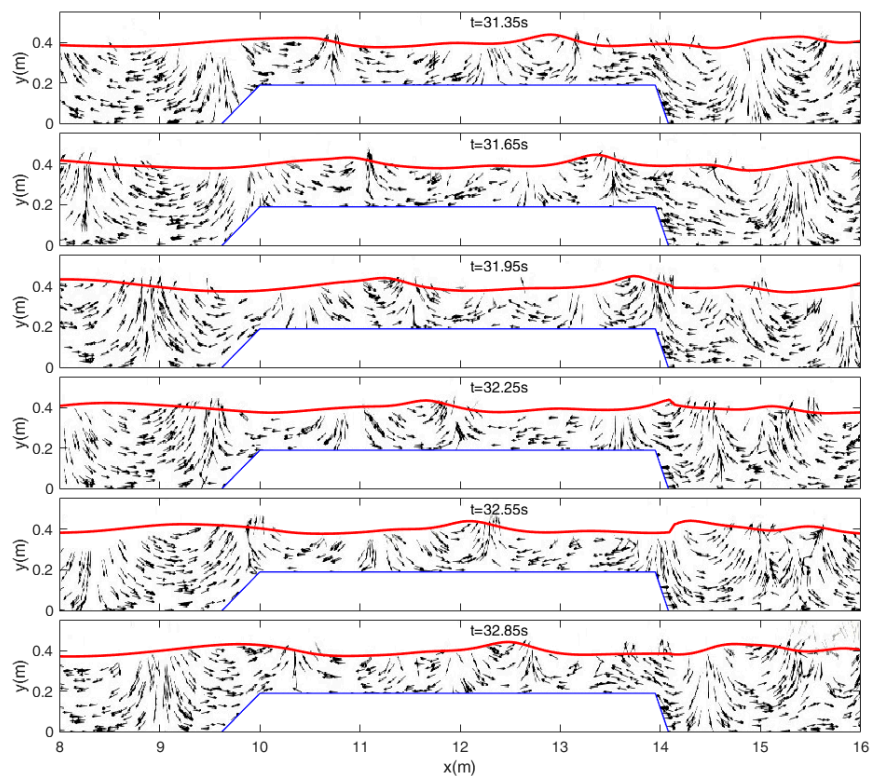


Figure 12. The flow field around impermeable submerged breakwater (Case 25).

These two figures show that the surface profile over impermeable breakwater displays a greater oscillation pattern, indicating a more intense nonlinearity, which is consistent with the findings shown in Figures 9 and 10. Outside of the permeable and impermeable structures, the general patterns of flow fields are nearly identical. The most noticeable difference can be found close to the breakwaters. As can be seen from Figure 11, there is a certain delay in the flow of water within the submerged breakwater caused by the change in wave height. The wave crest causes positive pressure at the top of the breakwater, which causes the water to enter the permeable breakwater, and the wave trough causes negative pressure at the top of the breakwater, which causes the water to flow out of the permeable breakwater. In contrast, the flow direction near the impermeable structure is tangent to the surface of the breakwater.

The pore distribution of permeable breakwaters is susceptible to turbulent flow phenomena. Figure 13 shows the turbulent kinetic energy distribution near the permeable breakwater in one cycle, and the comparison with the flow field in Figure 11 shows that the presence of the wave crest causes flow towards the permeable breakwater and causes an increase in the turbulence intensity in the seepage area. As the waves propagate over the submerged breakwater, the turbulent kinetic energy induced decays continuously, and when the wave crest propagates from the front of the breakwater ($t = 31.35$ s) to the middle of the breakwater top ($t = 32.85$ s), the turbulent kinetic energy intensity decreases from $0.005 \text{ m}^2/\text{s}^2$ to $0.0027 \text{ m}^2/\text{s}^2$, an attenuation of 46%. The attenuation of turbulent energy is mainly due to the water seeping into and out of the submerged breakwater as the wave propagates over the breakwater, resulting in a decrease in wave height, an attenuation of flow velocity, and a rapid decrease in turbulent energy.

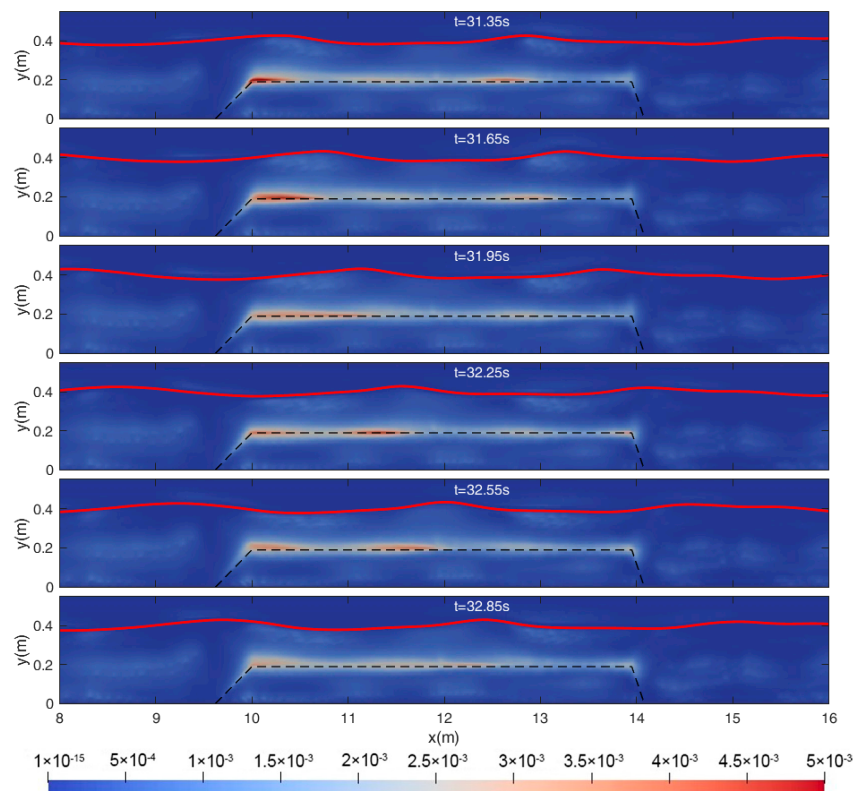


Figure 13. The turbulence kinetic energy around permeable submerged breakwater (Case 25).

Figure 14 shows the turbulent energy distribution near the impermeable breakwater in one cycle. Unlike the permeable breakwater, the turbulent energy intensity at the top of the impermeable breakwater at the junction with the water column is very low, so the wave attenuation is smaller on the impermeable breakwater. Due to the obvious vortex formed

at the front and back toe of the submerged breakwater, the turbulent energy intensity at the water bottom in front of the submerged breakwater and the water surface after the submerged breakwater is larger.

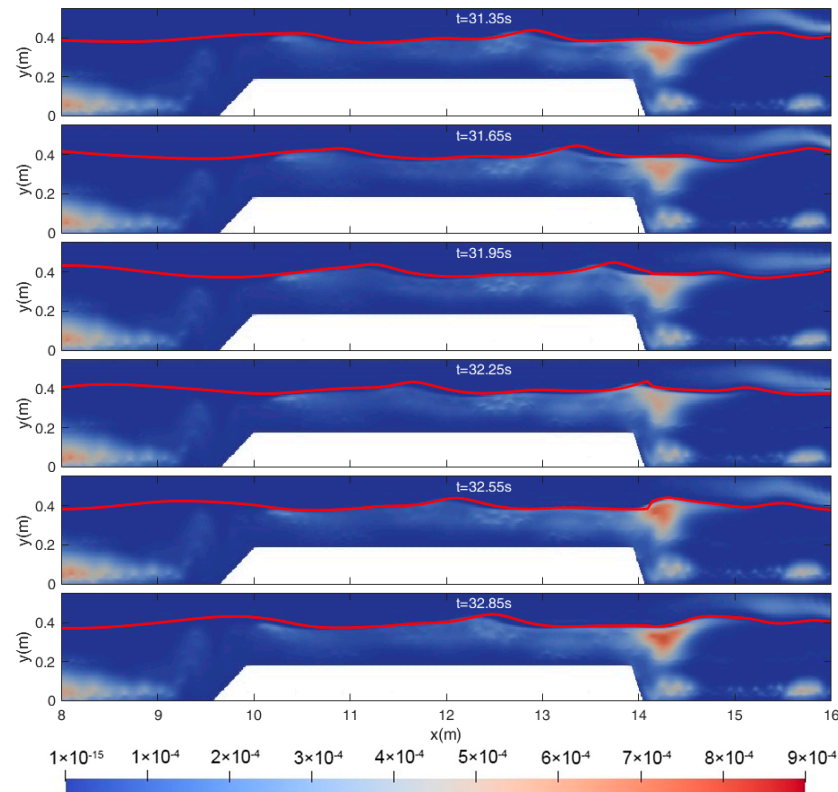


Figure 14. The turbulence kinetic energy around impermeable submerged breakwater (Case 25).

5.3. Further Discussion

The larger porosity of the permeable submerged breakwater means that more water enters the submerged breakwater, and the wave dissipation of the submerged breakwater is larger, but if we assume that the porosity is 1, this means that no submerged breakwater exists, and there is no wave dissipation; the wave dissipation will shift at a certain value of the porosity. Hieu and Tanimoto [47] pointed out that when the flow friction of the porous medium reaches the maximum, the wave energy dissipation also reaches the maximum. Zhang et al. [48] also analyzed the propagation process of isolated waves in a permeable submerged breakwater and pointed out that the maximum wave dissipation may occur in the submerged breakwater when the porosity is 0.6. For the wider permeable submerged breakwater proposed in this paper (with a width greater than 1 wavelength), there will also be an optimal porosity size. The wave height attenuation under different porosities was studied by a numerical model; the simulation conditions were consistent with Case 14 ($T = 1.5$ s, $H = 4$ cm, $D_1 = 30$ cm), the size of the submerged breakwater was unchanged, the median particle size of the porous media was 5 cm, and the porosity increased from 0.1 to 0.6. The submerged breakwater was located at the position of 10 m~14 m in the numerical flume, and the wave height attenuation on the submerged breakwater with different porosities is shown in Figure 15.

According to the experimental results in Figures 3 and 4, when the wave is unbroken, the wave height on the impermeable submerged breakwater increases slightly, while the wave height before and after the submerged breakwater is basically unchanged, so the transmission coefficients of the wave on the permeable submerged breakwater were mainly analyzed. As shown in the figure, the wave height attenuation rate and porosity are not simple linear relationships; with the increase in porosity, the wave height attenuation

rate shows a trend of first increasing and then decreasing. The porosity increased from 0.1 to 0.2, and the attenuation rate of wave height increased by 0.08, but as the porosity increased further to 0.6, the attenuation rate of wave height decreased by 0.28. The best wave dissipation can be achieved when the porosity of the permeable breakwater is around 0.2. Similar conclusions were also obtained in the study of Wu and Hsiao [6] where the transmission coefficient of the submerged breakwater increases and the dissipation coefficient decreases when the porosity is greater than 0.5.

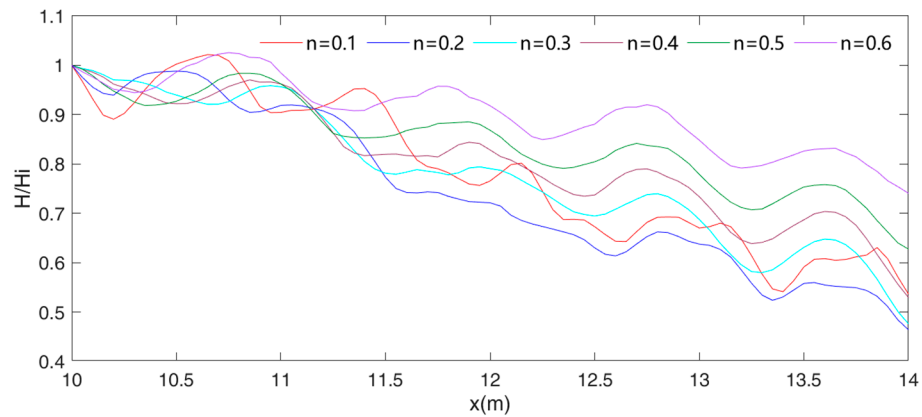


Figure 15. Attenuation of wave height over submerged breakwater with different porosity.

Figure 16 shows the distribution of turbulent energy near the permeable breakwater under different porosities. The turbulent energy is mainly distributed at the top of the wave-facing side of the breakwater, and the turbulent kinetic energy in the permeable breakwater gradually decreases with the increase of porosity, which leads to the weakening of the wave attenuation at porosity greater than 0.2.

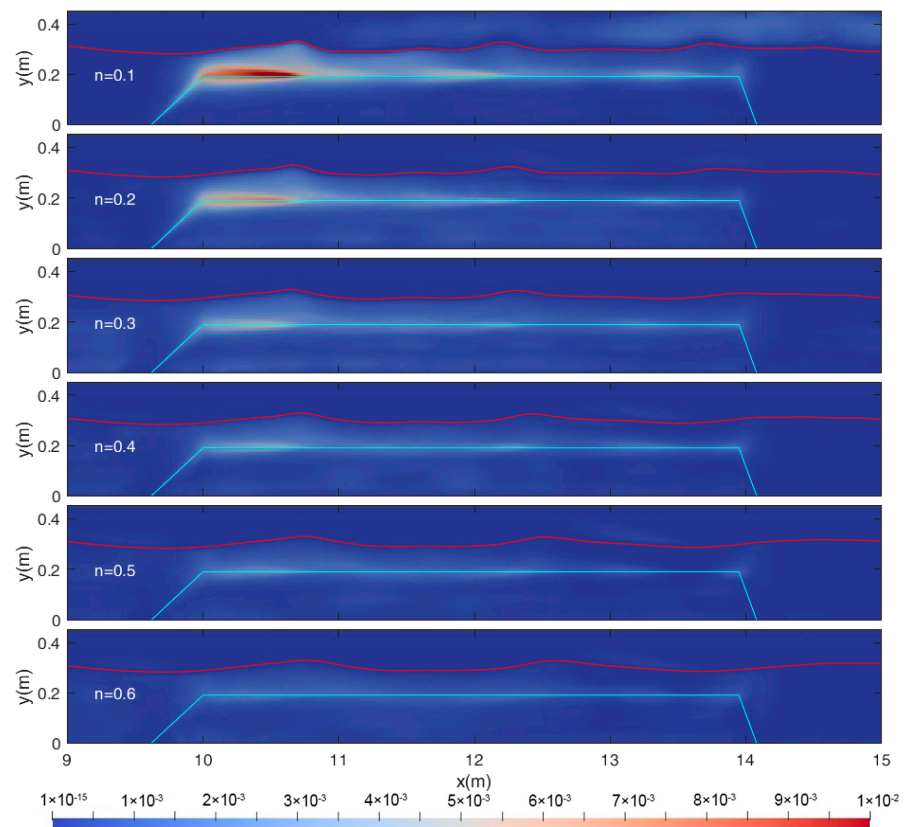


Figure 16. The turbulence kinetic energy around permeable submerged breakwater.

The wave dissipation effect can be improved by increasing the height of the submerged breakwater (Zhang et al. [48]), but higher submerged breakwaters have a large impact on both coastal hydrodynamics and water quality; therefore, increasing the width of the submerged breakwater rather than the height is used to achieve a better wave dissipation effect. In order to analyze the effect of the width of the permeable submerged breakwater on the transmission coefficient, the wave conditions of Case 14 ($T = 1.5$ s, $H = 4$ cm, $D_1 = 30$ cm) were simulated, keeping the porosity of the permeable submerged breakwater at 0.32 and the particle size of the porous medium at a 5 cm constant. The wave height attenuation on each submerged breakwater is shown in Figure 17, which shows that as the width of the permeable submerged breakwater increases, the wave height attenuation increases, and the transmission coefficient decreases. The effect of the width of the submerged breakwater on its wave dissipation capacity is predictable; when the width of the submerged breakwater becomes longer, the wave dissipation effect becomes stronger, resulting in greater wave attenuation.

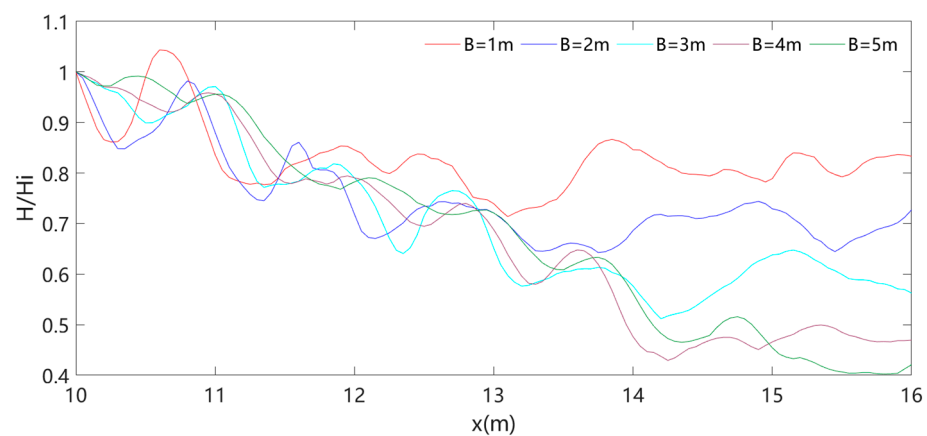


Figure 17. Attenuation of wave height on submerged breakwater.

The above results also confirm the conclusions of the isolated wave propagation study by Wu and Hsiao [6] on a permeable submerged breakwater. The influence of the width of the submerged permeable breakwater is much more significant because as the width of the breakwater increases, the speed of the waves decreases due to more wave energy being dissipated within the porous structure, and the energy transmission coefficient decreases.

6. Conclusions

This paper studies the nonlinear evolution and dissipation of non-breaking regular waves over a wide permeable submerged breakwater using a series of physical experiments and a validated olaFoam model. The main conclusions from this study can be drawn as follows:

- (1) Regular waves undergo significant nonlinear transformation over a wide impermeable submerged breakwater. The permeable submerged breakwater can effectively suppress the generation of harmonics and reduce their amplitudes when waves travel onto and along the breakwater.
- (2) The water depth at the top of the breakwater plays a key role in affecting the wave transmission coefficient. When the wavelength is close to or larger than the width of the top of the submerged breakwater, the wave transmission coefficient increases with the increase in relative wave height, whereas wave conditions with shallower water depth can achieve lower transmission coefficients under similar relative wave height conditions.
- (3) A large amount of turbulent kinetic energy is observed at the interface between the permeable submerged breakwater and the water body, which helps to dissipate wave energy. It is discovered that wave dissipation coefficients do not always increase

with increasing porosity. When the porosity exceeds a certain value, the dissipation coefficients decrease with increasing porosity, and the transmission coefficients of the submerged breakwater increase instead. For the wide permeable submerged breakwater considered in this paper, the wave dissipation capacity is greatest when the porosity is between 0.2 and 0.3. Better wave attenuation is achieved when the permeable submerged breakwater has a certain porosity and a large width.

- (4) olaFoam reasonably reproduces the measurements after carefully tuning the parameters and could provide more details of the flow field.

Future experimental and numerical investigations will be carried out for irregular waves. Wave breaking over the permeable breakwater is also intended to be considered, which complicates the hydrodynamics and deserves in-depth study.

Author Contributions: Conceptualization, P.W. and K.F.; methodology, P.W. and K.F.; software, P.W., K.F. and Z.L.; validation, P.W., K.F., Z.L., J.S. and G.W.; formal analysis, P.W., K.F., Z.L., J.S. and G.W.; resources, K.F. and Z.L.; data curation, J.S. and G.W.; writing—original draft preparation, P.W. and K.F.; writing—review and editing, P.W., K.F. and Z.L.; visualization, Z.L., J.S. and G.W.; supervision, P.W. and K.F.; project administration, P.W. All authors have read and agreed to the published version of the manuscript.

Funding: This research was funded by the National Key Research and Development Program of China (2022YFC3106101), and the National Natural Science Foundation of China (52071057, 52171247, and 51709054), and Open Research Project of Hebei Marine Ecological Restoration and Smart Ocean Monitoring Engineering Research Center (HBMESO2316).

Institutional Review Board Statement: Not applicable.

Informed Consent Statement: Not applicable.

Data Availability Statement: Not applicable.

Conflicts of Interest: The authors declare no conflict of interest.

References

1. Kubowicz-Grajewska, A. Morpholithodynamical changes of the beach and the nearshore zone under the impact of submerged breakwaters—A case study (Orłowo Cliff, the Southern Baltic). *Oceanologia* **2015**, *57*, 144–158. [[CrossRef](#)]
2. Lorenzoni, C.; Postacchini, M.; Brocchini, M.; Mancinelli, A. Experimental study of the short-term efficiency of different breakwater configurations on beach protection. *J. Ocean. Eng. Mar. Energy* **2016**, *2*, 195–210. [[CrossRef](#)]
3. Cappiotti, L. Converting emergent breakwaters into submerged breakwaters. *J. Coast. Res.* **2011**, *64*, 479–483.
4. Mori, E.; Cappiotti, L.; Aminti, P.L. *Laboratory Experiments for the Rehabilitation of Detached Breakwaters at Marina di Massa (ITALY)*; Coastal Structures 2007: (In 2 Volumes); World Scientific: Singapore, 2009; pp. 1421–1428.
5. Pranzini, E.; Rossi, L.; Lami, G.; Jackson, N.L.; Nordstrom, K.F. Reshaping beach morphology by modifying offshore breakwaters. *Ocean. Coast. Manag.* **2018**, *154*, 168–177. [[CrossRef](#)]
6. Wu, Y.T.; Hsiao, S.C. Propagation of solitary waves over a submerged permeable breakwater. *Coast. Eng.* **2013**, *81*, 1–18. [[CrossRef](#)]
7. Garcia, N.; Lara, J.L.; Losada, I.J. 2-D numerical analysis of near-field flow at low-crested permeable breakwaters. *Coast. Eng.* **2004**, *51*, 991–1020. [[CrossRef](#)]
8. Wu, D. *Study on the Transformation of Wave Propagation over the Submerged Breakwaters*; Dalian University of Technology: Dalian, China, 2012. (In Chinese)
9. Chang, K.A.; Hsu, T.J.; Liu, P.L.F. Vortex generation and evolution in water waves propagating over a submerged rectangular obstacle: Part II: Cnoidal waves. *Coast. Eng.* **2005**, *52*, 257–283. [[CrossRef](#)]
10. Li, A.; Liu, Y.; Liu, X. Analytical and experimental studies on water wave interaction with a submerged perforated quarter-circular caisson breakwater. *Appl. Ocean Res.* **2020**, *101*, 102267. [[CrossRef](#)]
11. Dattatri, J.; Raman, H.; Shankar, N.J. Performance characteristics of submerged breakwaters. *Coast. Eng. Proc.* **1978**, *16*, 130. [[CrossRef](#)]
12. Losada, I.J.; Patterson, M.D.; Losada, M.A. Harmonic generation past a submerged porous step. *Coast. Eng.* **1997**, *31*, 281–304. [[CrossRef](#)]
13. Ting, C.L.; Lin, M.C.; Cheng, C.Y. Porosity influences on non-breaking surface waves over permeable submerged breakwaters. *Coast. Eng.* **2004**, *50*, 213–224. [[CrossRef](#)]
14. Peng, Z.; Zou, Q.; Reeve, D.; Wang, B. Parameterisation and transformation of wave asymmetries over a low-crested breakwater. *Coast. Eng.* **2009**, *56*, 1123–1132. [[CrossRef](#)]
15. Zou, Q.; Peng, Z. Evolution of wave shape over a low-crested structure. *Coast. Eng.* **2011**, *58*, 478–488. [[CrossRef](#)]

16. Cruz, E.C.; Isobe, M.; Watanabe, A. Boussinesq equations for wave transformation on porous beds. *Coast. Eng.* **1997**, *30*, 125–156. [[CrossRef](#)]
17. Hsiao, S.-C.; Liu, P.; Chen, Y. Nonlinear water waves propagating over a permeable bed. *Proc. R. Soc. A Math. Phys. Eng. Sci.* **2002**, *458*, 1291–1322. [[CrossRef](#)]
18. Liu, Z.B.; Sun, Z.C.; Fang, K.Z. Mathematical model for wave propagation over a porous seabed and its numerical validation. *J. Dalian Univ. Technol.* **2013**, *53*, 417–422. (In Chinese)
19. Chen, Q. Fully nonlinear Boussinesq-type equations for waves and currents over porous beds. *J. Eng. Mech.* **2006**, *132*, 220–230. [[CrossRef](#)]
20. Hsiao, S.C.; Hu, K.C.; Hwung, H.H. Extended Boussinesq equations for water-wave propagation in porous media. *J. Eng. Mech.* **2010**, *136*, 625–640. [[CrossRef](#)]
21. Chondros, M.K.; Memos, C.D. A 2DH nonlinear Boussinesq-type wave model of improved dispersion, shoaling and wave generation characteristics. *Coast Eng.* **2014**, *91*, 99–122. [[CrossRef](#)]
22. Madsen, P.A.; Schäffer, H.A. Higher-order Boussinesq-type equations for surface gravity waves: Derivation and analysis. *Phil. Trans. Roy. Soc. Lond.* **1998**, *356*, 3123–3184. [[CrossRef](#)]
23. Metallinos, A.S.; Klonaris, G.T.; Memos, C.D.; Dimas, A.A. Hydrodynamic conditions in a submerged porous breakwater. *Ocean Eng.* **2019**, *172*, 712–725. [[CrossRef](#)]
24. Liu, P.L.-F.; Lin, P.; Chang, K.-A.; Sakakiyama, T. Numerical Modeling of Wave Interaction with Porous Structures. *J. Waterw. Port Coast. Ocean. Eng.* **1999**, *125*, 322–330. [[CrossRef](#)]
25. Hsu, T.-J.; Sakakiyama, T.; Liu, P.L.-F. A numerical model for wave motions and turbulence flows in front of a composite breakwater. *Coast. Eng.* **2002**, *46*, 25–50. [[CrossRef](#)]
26. Losada, I.; Lara, J.; Guanche, R.; Gonzalezondina, J. Numerical analysis of wave overtopping of rubble mound breakwaters. *Coast. Eng.* **2008**, *55*, 47–62. [[CrossRef](#)]
27. Lara, J.L.; Losada, I.J.; Maza, M.; Guanche, R. Breaking solitary wave evolution over a porous underwater step. *Coast. Eng.* **2011**, *58*, 837–850. [[CrossRef](#)]
28. Huang, C.J.; Chang, H.H.; Hwung, H.H. Structural permeability effects on the interaction of a solitary wave and a submerged breakwater. *Coast. Eng.* **2003**, *49*, 1–24. [[CrossRef](#)]
29. Jesus, M.D.; Lara, J.L.; Losada, I.J. Three-dimensional interaction of waves and porous coastal structures: Part I: Numerical model formulation. *Coast. Eng.* **2012**, *64*, 57–72. [[CrossRef](#)]
30. Higuera, P.; Lara, J.L.; Losada, I.J. Three-dimensional interaction of waves and porous coastal structures using OpenFOAM®. Part I: Formulation and validation. *Coast. Eng.* **2014**, *83*, 243–258. [[CrossRef](#)]
31. Lara, J.L.; Jesus, M.D.; Losada, I.J. Three-dimensional interaction of waves and porous coastal structures: Part II: Experimental validation. *Coast. Eng.* **2012**, *64*, 26–46. [[CrossRef](#)]
32. Wu, Y.T.; Yeh, C.L.; Hsiao, S.C. Three-dimensional numerical simulation on the interaction of solitary waves and porous breakwaters. *Coast. Eng.* **2014**, *85*, 12–29. [[CrossRef](#)]
33. Trulsen, K.; Raustol, A.; Jorde, S.; Rye, L.B. Extreme wave statistics of long-crested irregular waves over a shoal. *J. Fluid Mech.* **2020**, *882*, R2. [[CrossRef](#)]
34. Li, Y.; Zheng, Y.L.; Lin, Z.; Adcock, T.A.A.; van den Bremer, T.S. Surface wavepackets subject to an abrupt depth change. Part 1. Second-order theory. *J. Fluid Mech.* **2021**, *915*, A71. [[CrossRef](#)]
35. Trulsen, K.; Zeng, H.; Gramstad, O. Laboratory evidence of freak waves provoked by non-uniform bathymetry. *Phys. Fluid* **2012**, *24*, 097101. [[CrossRef](#)]
36. Li, Y.; Draycott, S.; Adcock, T.A.A.; van den Bremer, T.S. Surface wavepackets subject to an abrupt depth change. Part II: Experimental analysis. *J. Fluid Mech.* **2021**, *915*, A71. [[CrossRef](#)]
37. Zheng, Y.; Lin, Z.; Li, Y.; Adcock, T.A.A.; Li, Y.; van den Bremer, T.S. Fully nonlinear simulations of unidirectional extreme waves provoked by strong depth transitions: The effect of slope. *Phys. Rev. Fluids* **2020**, *5*, 064804. [[CrossRef](#)]
38. Lawrence, C.; Trulsen, K.; Gramstad, O. Statistical properties of wave kinematics in long-crested irregular waves propagating over non-uniform bathymetry. *Phys. Fluid* **2021**, *33*, 046601. [[CrossRef](#)]
39. Engelund, F. *On the Laminar and Turbulent Flow of Ground Water through Homogeneous Sand*; Transactions of the Danish Academy of Technical Sciences; Akademiet for de Tekniske Videnskaber: Copenhagen, Denmark, 1953.
40. Ven Gent, M.R.A. Porous Flow through Rubble-Mound Material. *J. Waterw. Port Coast. Ocean. Eng.* **1995**, *121*, 176–181. [[CrossRef](#)]
41. Jensen, B.; Jacobsen, N.G.; Christensen, E.D. Investigations on the porous media equations and resistance coefficients for coastal structures. *Coast. Eng.* **2014**, *84*, 56–72. [[CrossRef](#)]
42. Menter, F.; Ferreira, J.F.; Esch, T.; Konno, B. The SST Turbulence Model with Improved Wall Treatment for Heat Transfer Predictions in Gas Turbines. *Int. Gas Turbine Congr.* **2003**, *2003*, 1–7.
43. Larsen, B.E.; Fuhrman, D.R. On the over-production of turbulence beneath surface waves in Reynolds-averaged Navier-Stokes models. *J. Fluid Mech.* **2018**, *853*, 419–460. [[CrossRef](#)]
44. Mayer, S.; Madsen, P.A. Simulation of breaking waves in the surf zone using a Navier-Stokes solver. In *International Conference on Coastal Engineering*; ASCE: Sydney, Australia, 2000; pp. 928–941.
45. Devolder, B.; Troch, P.; Rauwoens, P. Performance of a buoyancy-modified k- ω and k- ω SST turbulence model for simulating wave breaking under regular waves using OpenFOAM®. *Coast. Eng.* **2018**, *138*, 49–65. [[CrossRef](#)]

46. Seabrook, S.R.; Hall, K.R. Wave Transmission at Submerged Rubble mound Breakwaters. *Coast. Eng.* **1998**, *1999*, 2000–2013.
47. Hieu, P.D.; Tanimoto, K. Verification of a vof-based two-phase flow model for wave breaking and wave–structure interactions. *Ocean. Eng.* **2006**, *33*, 1565–1588. [[CrossRef](#)]
48. Zhang, J.S.; Zheng, J.H.; Jeng, D.S.; Wang, G. Numerical simulation of solitary wave induced flow motion around a permeable submerged breakwater. *J. Appl. Math.* **2012**, *2012*, 1–14. [[CrossRef](#)]

Disclaimer/Publisher’s Note: The statements, opinions and data contained in all publications are solely those of the individual author(s) and contributor(s) and not of MDPI and/or the editor(s). MDPI and/or the editor(s) disclaim responsibility for any injury to people or property resulting from any ideas, methods, instructions or products referred to in the content.